# 3D-nanostructured boron-doped diamond for microelectrode array neural interfacing

Gaëlle Piret, Clément Hébert, Jean-Paul Mazellier, Lionel Rousseau, Emmanuel Scorsone, Myline Cottance, Gaelle Bazin Lissorgues, Marc O Heuschkel, Serge Picaud, P. Bergonzo, et al.

Biomaterials 53 (2015) 173–183

Contents lists available at ScienceDirect

Biomaterials

journal homepage: www.elsevier.com/locate/biomaterials

# 3D-nanostructured boron-doped diamond for microelectrode array neural interfacing

Gaëlle Piret [a, b, c, *, 1], Clément Hébert [d, *, 1], Jean-Paul Mazellier [e], Lionel Rousseau [f], Emmanuel Scorsone [d], Myline Cottance [f], Gaelle Lissorgues [f], Marc O. Heuschkel [g], Serge Picaud [h, i, j], Philippe Bergonzo [d], Blaise Yvert [a, b, c, *]

[a] INSERM, UA01, Clinatec Laboratory, Biomedical Research Center Edmond J. Safra, F-38 000 Grenoble, France
[b] Université Grenoble Alpes, UA01, Clinatec Laboratory, Biomedical Research Center Edmond J. Safra, F-38 000 Grenoble, France
[c] CEA, LETI, Clinatec, F-38000 Grenoble, France
[d] CEA, LIST, Diamond Sensors Laboratory, 91191 Gif-sur-Yvette, France
[e] Thales Research & Technology, Palaiseau, 91767 Cedex, France
[f] ESIEE-Paris, ESYCOM, University Paris EST, Cité Descartes BP99, Noisy-Le-Grand F-93160, France
[g] Qwane Biosciences SA, EPFL Innovation Park, CH-1015 Lausanne, Switzerland
[h] INSERM, U968, Institut de la Vision, Paris F-75012, France
[i] Sorbonne Universités, UPMC Univ Paris 06, UMR_S968, Institut de la Vision, Paris F-75012, France
[j] CNRS UMR7210, Institut de la Vision, Paris 75012, France

ARTICLE INFO

*Article history:*
Received 24 November 2014
Received in revised form
21 January 2015
Accepted 1 February 2015
Available online

*Keywords:*
Neural recording
Neural prosthesis
Electrode
Biocompatibility
Electrophysiology
Electrical stimulation

ABSTRACT

The electrode material is a key element in the design of long-term neural implants and neuroprostheses. To date, the ideal electrode material offering high longevity, biocompatibility, low-noise recording and high stimulation capabilities remains to be found. We show that 3D-nanostructured boron doped diamond (BDD), an innovative material consisting in a chemically stable material with a high aspect ratio structure obtained by encapsulation of a carbon nanotube template within two BDD nanolayers, allows neural cell attachment, survival and neurite extension. Further, we developed arrays of 20-μm-diameter 3D-nanostructured BDD microelectrodes for neural interfacing. These microelectrodes exhibited low impedances and low intrinsic recording noise levels. In particular, they allowed the detection of low amplitude (10–20 μV) local-field potentials, single units and multiunit bursts neural activity in both acute whole embryonic hindbrain-spinal cord preparations and long-term hippocampal cell cultures. Also, cyclic voltammetry measurements showed a wide potential window of about 3 V and a charge storage capacity of 10 mC.cm$^{-2}$, showing high potentiality of this material for neural stimulation. These results demonstrate the attractiveness of 3D-nanostructured BDD as a novel material for neural interfacing, with potential applications for the design of biocompatible neural implants for the exploration and rehabilitation of the nervous system.



## 1. Introduction

Neuroengineering more efficient neural interfaces is crucial to better explore neural networks [1–6] and to offer advanced clinical rehabilitation solutions based on neural prosthesis and brain-computer interfaces to target pathologies such as hearing loss [7], pathological tremors [8], visual impairments [9,10], or paralysis [11–15]. These devices make use of microelectrode arrays (MEAs) [16–19] to record the electrical activity from neural structures and can deliver electrical microstimulation in these structures to restore previously lost functions. One way to improve such systems is to increase their electrode number and density. For instance, increasing the number of recorded channels improves the efficiency of brain machine interfaces [14] and neural prosthesis [20]. In the case of retinal prosthesis, Nirenberg et al. have shown that driving a high density stimulator network with the retina's neural code could considerably rise the reconstructed image resolution [21]. Also, probing the electrical activity of neural circuits at multiple locations with miniaturized microelectrodes is expected to

* Corresponding authors. Clinatec UA01, Biomedical Research Center Edmond J. Safra, CEA-LETI-Minatec Campus, 17 rue des Martyrs, 38054 Grenoble Cedex 09, France. Tel.: +33 4 38 78 91 38; fax: +33 4 38 78 53 55.
*E-mail addresses:* gaelle.offranc-piret@inserm.fr (G. Piret), clement.hebert@cea.fr (C. Hébert), blaise.yvert@inserm.fr (B. Yvert).
[1] These authors contributed equally to this work.

http://dx.doi.org/10.1016/j.biomaterials.2015.02.021

decipher their dynamics beyond characterizing their structural aspects [22–24]. However, increasing the density of microelectrodes implies the reduction of their dimensions [22,24–27], which has two major consequences [28]. First, small diameter electrodes lead to a high intrinsic noise level and thus low signal to noise ratio, precluding sensitive neural recordings. Second, charge injection capacity is reduced, hindering efficient electrical neural stimulation. Therefore, a current challenge is to find new biocompatible and more efficient electrode materials to optimize the electrode–tissue interface [3,29].

Boron doped diamond (BDD) is one of the materials of choice for electrodes of long-term neural implants since it combines properties of biocompatibility [30–39], chemical inertness [40], and structural stability at current charge densities typically applied for neural stimulation [41,42]. Previous studies have shown that BDD MEAs can successfully be used to resolve electrochemical signals with high-time resolution from whole living cells [43] or microareas of functional neuroendocrine cells [44]. Moreover, it exhibits a wide potential window in aqueous media [45], making it particularly suitable for neural stimulation [46–48]. Although BDD normally suffers from a low double layer capacitance and high impedance in comparison to other competitive materials for neural interfacing, Hebert et al. recently proposed an innovative solution where the specific surface area of BDD electrodes is increased using vertically aligned carbon nanotubes (VACNTs) as a template interlayer [49], a strategy in line with previous studies using nanostructuration strategies to enhance the electrode performance for neural recording and stimulation [28,50–55].

Moreover, the advantage of using nanostructures to modify the electrode geometry seems to be two-fold. First, *in vitro* studies have indeed evidenced that specific nanotopographies can support the sprouting of neurons from the central and peripheral nervous system without favoring the spread of glial cells [56–61]. Second, the use of nanostructures appears to be beneficial to interface neural tissues [61–65].

There has been only few attempts of neural recording using BDD microelectrodes [66–68], however yielding to rather high recording noise due to the high interface impedance and low double-layer capacitance of diamond. Moreover, Halpern et al. have shown that a single needle microelectrode coated with BDD could successfully be used to stimulated single neurons [46]. Such technology has however not yet been integrated into microelectrode arrays. Here, we investigated the possible use of 3D-nanostructured BDD as a material for efficient bidirectional neural interfacing in a configuration of 20-μm-diameter-microelectrode arrays. For this, the suitability of nanostructured BDD for culturing embryonic neural cells was first evaluated. We then developed a microfabrication process to design microelectrode arrays made of either conventional BDD or 3D-nanostructured BDD, consisting of vertically aligned carbon nanotubes (VACNTs) inter-layer template embedded in two BDD nanolayers. We finally evaluated the performance of both types of BDD microelectrodes for *ex vivo* neural tissue *and in vitro* cell culture recording and stimulation.

## 2. Methods

All experimental protocols conformed to recommendations of the European Community Council Directive of November 24, 1986 (86/609/EEC) and local French legislation for care and use of laboratory animals, and have been approved by the Bordeaux ethical committee for experimental research (Approval No A5012082).

### 2.1. Hippocampal and spinal cord cell cultures on 3D-nanostructured BDD films

#### 2.1.1. Fabrication of BDD substrates

BDD films were produced on silicon substrates. Detonation diamond nanoparticules (6-nm) dispersed in water (0.1% wg) were spread by spin coating on these substrates. Then a 600-nm-thick nano-crystalline diamond film was grown at low temperature in a AX6500X Microwave Plasma Chemical Vapor Deposition (MPCVD) system (Seki Technotron Corp.). The growth was performed during 10 h under the following parameters: MW power of 2.6 kW, temperature of 650 °C, pressure of 26 mbar, gas concentration: 1% methane in approx. 99% hydrogen. Trimethylboron was added to the gas phase as dopant so that the resulting Boron concentration in the diamond film was approximately $2.10^{21}$ at.cm$^{-3}$ as determined by Secondary Ion Mass Spectrometry measurements. This was found to be optimum in terms of electrode performance [69]. Surfaces were then oxygenated using an ozone treatment during 2 h in order to obtain an oxygen-terminated BDD and thus a hydrophilic surface.

#### 2.1.2. Fabrication of 3D-nanostructured BDD substrates

VACNTs were grown on BDD films, and then coated with a second BDD film. The full fabrication process has been described previously [49]. In brief, a 7 nm nickel layer was deposited on the diamond surface by e-beam evaporation and turned into 50 nm nanoparticles by heating at 700 °C for 3 min. The samples are then transferred into a plasma enhanced CVD reactor ("Black Magic" AIXTRON) where the nickel particles are used for the catalysis of 3-μm-long vertically aligned carbon nanotubes. These VACNTs are then coated with a layer of 25 nm diamond particles using an electrostatic grafting method described elsewhere [70]. Finally the diamond seeds were grown in a home-made MPCVD reactor until a BDD thin film of 50 nm was obtained on the bundles. Boron concentration in this case was also $2.10^{21}$ at.cm$^{-3}$. Surfaces were then oxygenated using an ozone treatment during 2 h in order to obtain an oxygen-terminated BDD and thus a hydrophilic surface.

#### 2.1.3. Spinal cord and hippocampal cell cultures

A digestion solution was prepared containing papain (30 Units/mL, Roche Life Science, code 10108014001) diluted at 0.1 mg/mL (3 Units/mL) and L-cysteine (Sigma Aldrich; code C7477) at 0.5 μg/mL in Neurobasal Medium (1×, Gibco Life Technologie; code 21103-049). The digestion solution was incubated at 37 °C during 10 min, filtered with a 0.22-μm-pore filter (SARSTEDT, Germany; code 83-1826-001) and used within 1 h. The hippocampi of both hemispheres of four E14.5 OF1 mice (Charles River, l'Arbresle, France) embryos were dissected and collected in a dissection medium [F-12 Nut Mix (Ham) medium with 2% of L-glutamine-penicillin-streptomycin (Sigma Aldrich, code G6784) and 1% of Gentamycin (Gibco Life Technologie; code 15710_049)]. Another E14.5 mouse embryo was decapitated, its spinal cord below the medulla was dissected and collected in the same dissection medium. Each tissue type was then treated separately but using the same procedure. The tissue was digested in a falcon tube for 30 min at 37 °C, carefully rinsed with 3 × 3 mL Neurobasal medium. Subsequently, 3 mL of culture medium [Neurobasal medium with 0.5% of L-glutamine-penicillin-streptomycin (Sigma Aldrich, code G6784), 0.25% of Gentamycin (Gibco Life Technologie; code 15710_049), 1% of Glutamax (Gibco Life Technologie; code 35050_038) and 1% of B27-supplement (Invitrogen Life Technologies; code 17504-044)] were added to the tissue, which was then gently triturated mechanically. The suspension was then spun down for 5 min at 1220 rpm at 20 °C (Eppendorf AG, Centrifuge 5810R). The supernatant was removed and the cell pellet was re-suspended in 3 mL of culture medium, dissociated mechanically and respun down. The cell pellet was then resuspended again in 800 μL of culture medium and passed through a 40 μm cell strainer (Biologix Research, ref 15–1040). 100 μL were then seeded onto the 3D-nanostructured BDD MEA and onto each substrate type. Before cell seeding, substrates were placed overnight in an oven at 60 °C, then incubated in 70% ethanol for 10 min, air-dried overnight, and finally placed separately in one well of a sterile 12-well plate (Nunc, Cat No 150628). No chemical coating was performed to augment cell adhesion so as to evaluate the bare material and the effect of the 3D-nanostructured BDD topography compared to the conventional BDD one. The plate was placed in the incubator during 15 min in order to allow for cell seeding. Further, 1.9 mL of culture medium were added to each well. Cultures were performed on different days and on 9 replicates of each substrate type.

#### 2.1.4. Immunocytochemistry and fluorescence microscopy

Following 8 DIV, the cultured cells were fixed in 4% paraformaldehyde (PFA) in PBS (10 mM), rinsed 3 x 10 min in PBS (10 mM, pH 7.2), and then blocked and permeabilized by pre-incubation for 30 min at room temperature with PBS (10 mM, pH 7.2) containing 0.25% Triton X-100 (PBS-T) and 2% bovine serum albumin (BSA). Cells were subsequently incubated for 60 min at room temperature with a mouse monoclonal antibody against β-tubulin, isotype III (Covance, MRB435P0100; 1:500 in PBS-T 1% BSA) followed by three 10 min washes with PBS-T with 1% BSA. The cells were further incubated with the secondary antibody: Alexa Fluor 488 goat anti-rabbit (Invitrogen; ref A11008) at 1:1000 for 60 min at room temperature, followed by three 10 min washes with PBS-T with 1% BSA. Cell samples were mounted with Slowfade gold antifade reagent with DAPI (Invitrogen molecular probes, 536938) examined with a wide field fluorescence microscope (Olympus I81) using a plan-neofluar objective (20×).

### 2.2. Fabrication of conventional BDD and 3D-nanostructured BDD MEAs

#### 2.2.1. Conventional BDD MEA

The fabrication process of diamond MEAs is shown in Fig. 1A. Planar 60-channel MEAs were developed with electrodes arranged in a 4 × 15 layout without corners

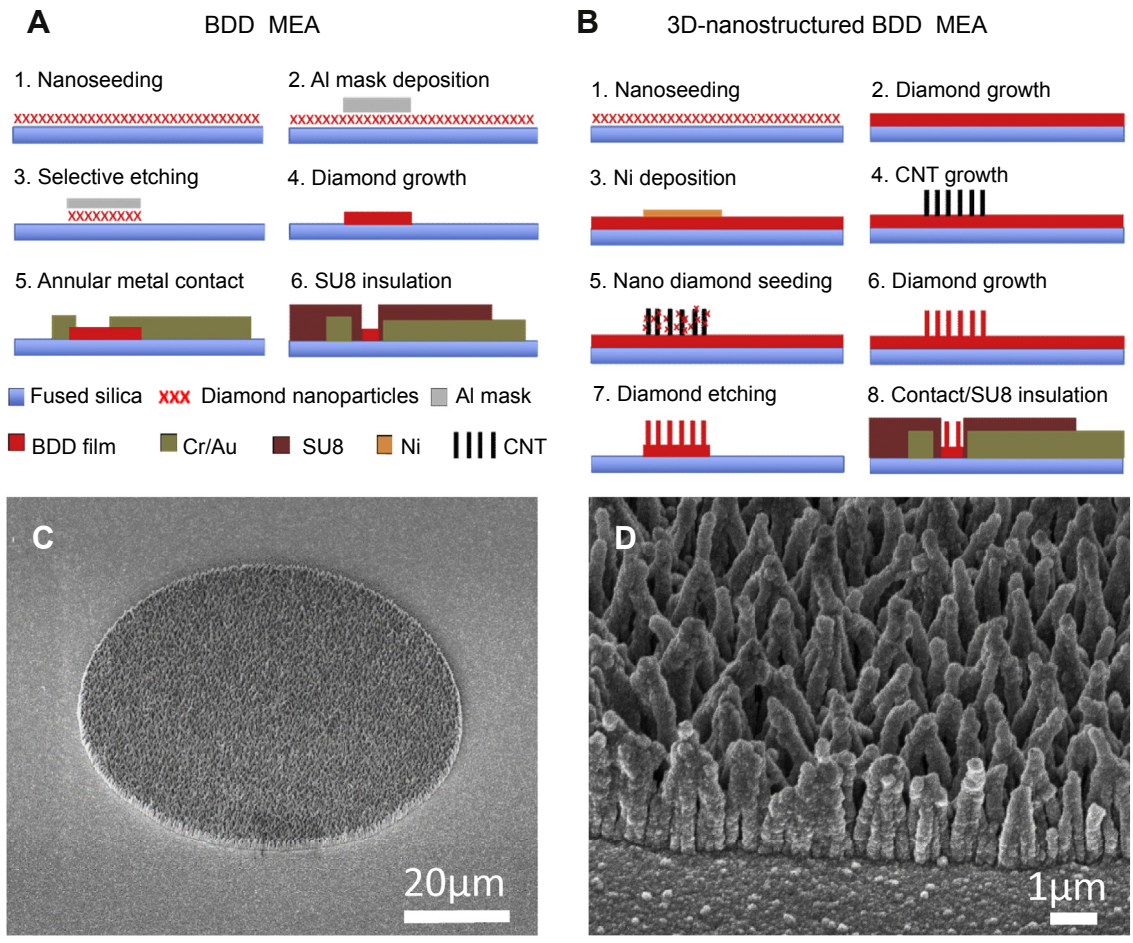


**Fig. 1.** Processing steps for microfabrication of A) the BDD MEA and B) the 3D-nanostructured BDD MEA. Scanning electron microscopy (SEM) picture of the 3D-nanostructured BDD at the step 6 of the MEA fabrication C) at low magnification and D) at a higher magnification at the interface of the BDD and the 3D-nanostructured BDD. The opening of the SU8 insulation layer will define the 20-µm-diameter of the electrode in the last step 8.

covering an area of 900 × 12600 $\mu m^2$ specifically adapted to the geometry of embryonic hindbrain-spinal cord preparations (Fig. S1A and Fig. 4A), and also with electrodes arranged in a 1 × 60 layout with a 150-µm spacing (Fig. S1B). To fabricate the arrays, an innovative approach was developed. At first, detonation diamond nanoparticles were spread onto a 4 inch fused silica (this substrate was used to avoid any electrical cross talk between the electrodes) using a process described earlier [71] (Step 1). Next, an aluminum layer, composed of 80-µm disks, was deposited to define the electrode patterns by photolithography (using the AZ4562 photoresist and AZ 351 B developer) (Step 2) and the diamond nanoparticles outside these protected areas were etched away using Reactive Ion Etching (RIE) under a pure oxygen plasma (Step 3). The aluminum hard mask was then chemically removed to reveal the diamond nanoparticles patterns, from which diamond electrodes were grown using Microwave *Plasma Enhanced Chemical Vapor Deposition* (MPECVD) in a diamond growth reactor (Seki AX6500) housing a gas mixture of methane, hydrogen, and trimethylboron. The fabricated diamond electrodes exhibited a thickness of 500 nm (Step 4). The electrodes were then individually contacted by depositing 10/150-nm Cr/Au metal tracks using lift-off with AZ nLof 2020 (MicroChemicals GmbH, Germany) as photoresist material. Contact to the electrodes was achieved by depositing a metal ring across the edges of the electrodes with a 5-µm overlap (Step 5). Finally a 2-µm-thick SU8 layer (MicroChem, USA) was deposited onto the substrate in order to isolate the metal tracks from the electrolyte solution and opened with SU8 developer to define the 20-µm-diameter of the microelectrode (Step 6).

### 2.2.2. 3D-nanostructured BDD MEAs

We recently reported on enhanced electrochemical properties of the BDD electrode using a template of carbon nanotubes scaffolds [49]. This technology was integrated on the MEA fabrication using the process described in Fig. 1B. The first two steps consist in growing a boron doped diamond layer from diamond seeds on the fused silica (this substrate was used to avoid any cross talk between the electrodes). Then an 8-nm-thick nickel layer was selectively deposited at the locations of the future electrodes (step 3). This metallic layer was used as a catalyst for the growth of an inter-layer of 3 µm vertically aligned carbon nanotubes (VACNTs) using PECVD after a growth time of 20 min (step 4). The VACNTs were cleaned in hot aqua regia [HCl(Sigma Aldrich):$HNO_3$(Merck), 3:1] to remove the catalyst that eventually remained at the tip of the VACNTs. The whole wafer was then coated with a highly dense nanodiamond layer to fully embed the VACNTs in the subsequent diamond growth step (step 5). A 50 nm boron doped diamond coating was performed with soft growth parameters as described in our previous study [49] (step 6, Fig. 1B–D). The result is the formation of a 3D-nanostructured BDD structure that has the shape of bundles as shown on Fig. 1D. The electrodes were locally masked with an aluminum layer using the AZ4562 photoresist and AZ 351 B developer. The boron doped diamond that grew outside of the electrodes was etched away using RIE under a pure oxygen plasma, and the aluminum mask was chemically removed (step 7). The electrodes were then individually contacted by depositing 10/150-nm Cr/Au metal tracks using lift-off with AZ nLof 2020 (MicroChemicals GmbH, Germany) as photoresist material. Contacts to the electrodes were achieved by depositing a metal ring across the edges of the electrodes with a 5 µm overlap. Finally a 2-µm-thick SU8 layer (MicroChem, USA) was deposited onto the substrate in order to isolate the metal tracks from the electrolyte solution and opened with SU8 developer to define the 20-µm-diameter of the microelectrode (Step 8, and see Fig. S1C).

### 2.3. Cyclic voltammetry

Ultrapure deionised (DI) water (Millipore Direct Q3) was used to prepare all solutions. For electrochemical activation and potential window measurement of the electrodes using cyclic voltammetry (CV), four solution were prepared: an aqueous solution of phosphate buffered Saline (PBS, Sigma Aldrich), a phosphate buffer prepared without NaCl, an artificial cerebrospinal fluid solution (aCSF) and lithium perchlorate ($LiClO_4$, Sigma Aldrich) at 0.5 mM. The CV was performed using a Biologic SP200 potentiostat in a three-electrode setup where the studied

microelectrode was the working electrode, a platinum wire the pseudo-reference electrode, and a platinum mesh the counter electrode.

### 2.4. Microelectrode impedance measurements

Electrochemical impedance spectroscopy (EIS) was performed in PBS and $LiClO_4$ over a frequency range from 0.1 Hz to 1 MHz with logarithmic point spacing and potential amplitude of 0.01 V rms while the diamond electrode was maintained at open circuit potential. The EIS was performed using a Biologic SP200 potentiostat in a three-electrode setup where the studied microelectrode was the working electrode, a platinum wire the pseudo-reference electrode, and a platinum mesh the counter electrode. Impedance measurements were also performed at 1 kHz using either a IMP-I Electrode Impedance Tester from Bak Electronics Inc (Mount Airy, USA) or a NanoZ (Multi Channel Systems GmbH, Reutlingen, Germany).

### 2.5. Microelectrode intrinsic noise measurements

To measure the intrinsic noise level of the electrodes, the electrical potential was recorded for 1 min in artificial cerebrospinal fluid (aCSF) between each microelectrode and an Ag/AgCl ground electrode pellet. The aCSF was composed of NaCl (113 mM), KCl (4.5 mM), $CaCl_2{-}2H_2O$ (2 mM), $MgCl_2{-}6H_2O$ (1 mM), $NaHCO_3$ (25 mM), $NaH_2PO_4H_2O$ (1 mM) and D-Glucose (11 mM). Signals were 1100 × amplified and band-pass filtered between 1 Hz and 3 kHz using MCS MEA1060-Up-BC filter amplifiers from Multi Channel Systems GmbH (Reutlingen, Germany). Data were acquired at 10 kHz using two synchronized CED Power1401 AD converters and the Spike2 v7 software from Cambridge Electronic Design (Cambridge, England). The standard deviation of the signal $\sigma_s$ was then calculated over the 1-min recording for each electrode of the array. Because this noise level was composed of both the intrinsic noise level of the electrodes $\sigma_e$ and the electronic noise level of the amplifiers $\sigma_a$, we assumed statistical independence of these two noise sources and estimated the intrinsic noise level $\sigma_e$ of each electrode as: $\sigma_e = \sqrt{\sigma_s^2 - \sigma_a^2}$, where $\sigma_a$ (=1.42 μV) was measured for each channel with the amplifier inputs connected to the ground. Noise evaluation was performed for conventional BDD microelectrodes, 3D-nanostructured BDD microelectrodes, as well as platinum and black platinum microelectrodes (commercially available from QWANE). Noise evaluation was also performed after physical cleaning of the MEA to assess its mechanical robustness. For this purpose, the MEA chamber was filled with a standard housekeeping dishwashing detergent (Paic citron) and the array was brushed using a soft painting brush. This procedure was repeated 10 times after which the noise was recorded again.

### 2.6. Neural recording and stimulation

#### 2.6.1. Acute embryonic spinal cord recording and stimulation

To test the performance of BDD microelectrodes for neural recordings, we considered a whole acute embryonic mouse hindbrain-spinal cord preparation. Indeed this preparation displays rhythmic activity occurring every few minutes as episodes consisting of local field potentials (LFPs) and bursts of spikes, and is particularly suitable to assess the performances of the MEA in terms of sensitivity since the signals include spikes of relatively small amplitudes typically around 10–20 μV [28,72]. This is due to the high impedance of the immature cells in this preparation [73] thus requiring small trans-membrane currents to be depolarized. E14.5 embryos were surgically removed from pregnant OF1 mice (Charles River Laboratories, L'Arbresle, France), previously killed by cervical dislocation. Embryos were decapitated and their whole spinal cord and hindbrain were dissected in aCSF gassed with carbogen (95% $O_2$, 5% $CO_2$), meninges were removed, and the neural tube was opened along the rostro–caudal axis (open-book preparation). The embryonic hindbrain-spinal cord preparation was then placed over the MEA (Fig. 4A) and superfused with physiological liquid, gassed with carbogen. A plastic net with small holes (70 × 70 $\mu m^2$) was laid on the neural tissue, in order to achieve a tight and uniform contact with the microelectrodes. Signals were x1100 amplified and bandpass filtered between 1 Hz and 3 kHz using MCS MEA1060-Up-BC filter amplifiers from Multi Channel Systems (Reutlingen, Germany). Data were acquired at 10 kHz using two synchronized CED Power1401 AD converters and the Spike2 v6 software from Cambridge Electronic Design (Cambridge, England). Rhythmic activity of this immature preparation was recorded for several hours at room temperature. LFP activity was obtained by smoothing the raw signals with a 200-ms time window. Spiking activity was extracted as follows: for each data sample, two moving averages of the signal computed over a 10-ms (DC removing) and a 1-ms (smoothing) time windows centered on this sample were subtracted from the raw data. The MEA was cleaned and used several times without any increase of the noise level, nor degradation of the performances of the BDD microelectrodes to be observed.

#### 2.6.2. Long-term hippocampal cell culture recording and stimulation

Following 14 DIV, the cells cultured on the 3D-nanostructured BDD MEA were superfused with physiological liquid, gassed with carbogen and recorded for hours at room temperature. As for the embryonic spinal cord recording, signals were x1100-amplified, bandpass filtered between 1 Hz and 3 kHz and acquired at 10 kHz. Spiking activity was extracted as described above for acute recordings.

## 3. Results

### 3.1. Hippocampal and spinal cord cell cultures on 3D-nanostructured BDD substrates

Cultures of hippocampal and spinal cord cells were used to evaluate the biocompatibility of the new 3D-nanostructured BDD substrate, fabricated with a protocol recently published by Hébert et al. [49], and presenting a novel 3D surface topography different from that of conventional BDD substrates (Fig. 2A and B). Cultures on 3D-nanostructured BDD substrates were compared to cultures on conventional BDD substrates, already known to be suitable for neural cultures [30–39]. The cell attachment and distribution was assessed using DAPI to stain cell nuclei. The cell ability to express the neuron-specific marker β-tubulin III and their neurite extension were also investigated. After 8 DIV, although cells were passed through a cell strainer just before cell seeding on the studied substrates, clusters and single cells were found to attach and extend neurites on both substrate types in both cell culture types (Fig. 2C–F). Similarly for the hippocampal cell culture and for the spinal cord cell culture, cells were found to express β-tubulin III and no difference in their neurite lengths could be observed on 3D-nanostructured BDD substrates (Fig. 2D and F) when compared with conventional BDD substrates (Fig. 2C and E).

### 3.2. Characterization of 3D-nanostructured BDD MEAs

The fabricated MEAs were characterized using cyclic voltammetry and impedance spectroscopy. Fig. 3A and B display three CV plots corresponding to 20 μm diameter conventional BDD microelectrodes measured in $LiClO_4$ (black dotted), and to 20 μm diameter 3D-nanostructured BDD microelectrodes measured in $LiClO_4$ (red) and in PBS (green). Within the 3–3.5 V wide potential window, a 3D-nanostructured BDD microelectrode leads to double layer capacitive currents approximately 44 times greater than values probed on conventional BDD microelectrodes. Indeed, the double layer capacitance ($C_{dl}$) as well as the charge storage capacity (CSC) of both electrode types can be deduced using the two following formula; $C_{dl} = \frac{\Delta i}{2\nu}$ and $CSC = \frac{1}{\nu}\int i_a dV$ where $\Delta i$ is the difference between the cathodic and anodic currents at the open circuit potential, $\nu$ is the scan speed, $i_a$ the anodic current density and V is the scanning potential. Hence, in $LiClO_4$, a conventional BDD microelectrode exhibits a double layer capacitance of 70 μF $cm^{-2}$ and a CSC of 220 μC $cm^{-2}$ whereas a 3D-nanostructured BDD microelectrode exhibits a double layer capacitance of 3 mF $cm^{-2}$ and a CSC of 10 mC $cm^{-2}$ (for a potential window of 3.3 V). In PBS, the structured diamond presents a large peak at 1.3 V and a lower anodic current (260 μA, Fig. 3B), reducing the potential window and inducing a double layer capacitance of 2.6 mF $cm^{-2}$ and a CSC of 6.8 mC $cm^{-2}$ (for a potential window of 2.6 V). This large peak at 1.3 V can also be found when performing CV measurements in aCSF (Fig. S2A). However, it is not visible when aCSF is replaced by a phosphate buffer, free of NaCl (Fig. S2B). Fig. 3C and D show the Bode representation of the typical impedance spectra for one conventional BDD microelectrode (black dotted) and one 3D-nanostructured BDD microelectrode (red) in PBS. These figures show that the impedance modulus is significantly lower (approximately 40 times) for the 3D-nanostructured BDD microelectrode, which corroborates the larger double layer capacitance observed using cyclic voltammetry. The lower phase at high frequency for the 3D-nanostructured BDD microelectrode indicates the lower cut-off frequency of this interface, a direct result of its higher capacitance when compared with conventional BDD microelectrodes.

Fig. 3E presents the impedance measurements at 1 KHz for all microelectrodes of one MEA as recorded in LiClO4, and thus

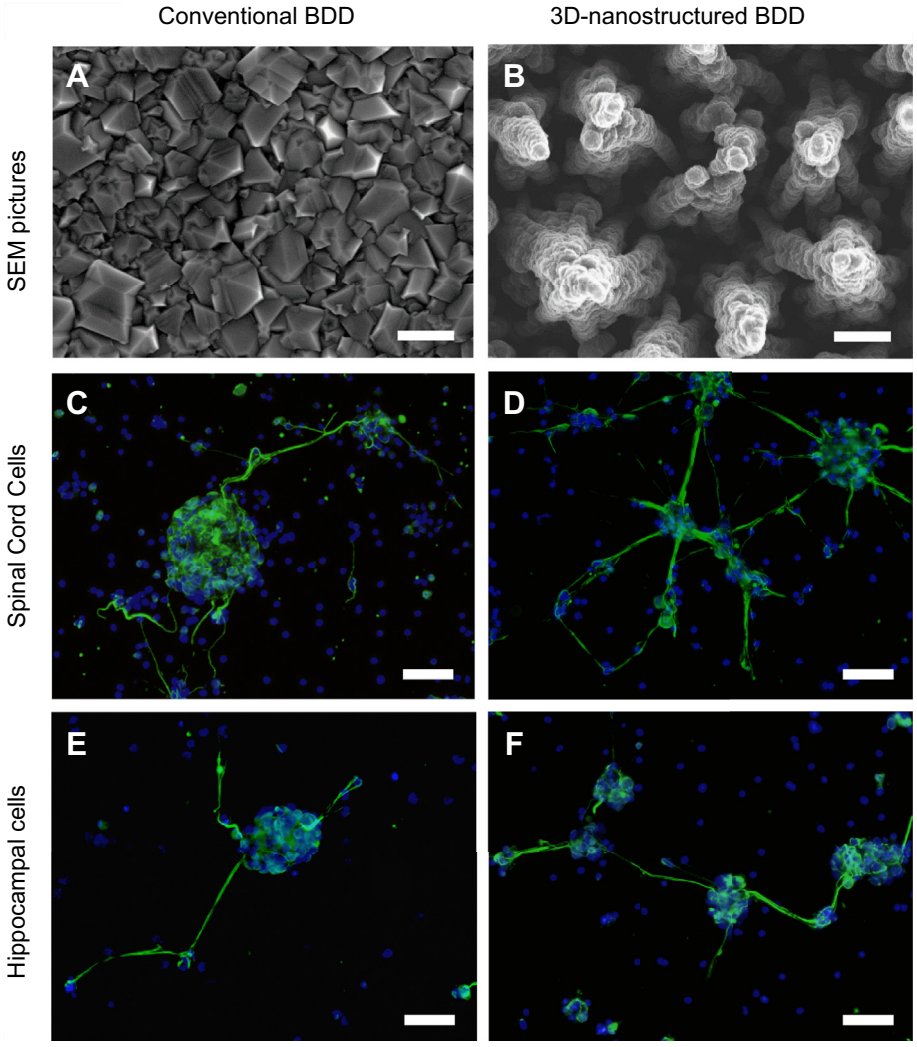


**Fig. 2.** SEM images showing a top view of A) BDD and of B) 3D-nanostructured BDD. Scale bar, 600 nm. Fluorescence microscopy pictures with nuclei labeled with DAPI (in Blue) and neurons labeled with β-tubulin III (in green) of spinal cord cells at 8 DIV on C) a BDD substrate and on D) a 3D-nanostructured BDD substrate, and of hippocampal cells at 8 DIV, and on E) a BDD substrate, and F) a 3D-nanostructured BDD substrate. Scale bar 50 μm. (For interpretation of the references to color in this figure legend, the reader is referred to the web version of this article.)

providing a view of the microfabrication process steadiness. There is indeed a small dispersion of the impedance modulus around 50 kΩ with more than 75% of the microelectrodes displaying an impedance modulus below 100 kΩ. The intrinsic noise level was recorded for conventional and 3D-nanostructured BDD MEAs. As reported in Fig. 3F, the median noise level of 3D-nanostructured BDD microelectrodes was found to be 3.1 μV. This is lower than the 6.9 μV found for Pt microelectrodes and considerably lower than the 10.7 μV found for conventional BDD microelectrodes. The smallest noise corresponds to black Pt microelectrodes showing a noise of 2.0 μV. As black platinum microelectrodes are highly friable [28], we also assessed the mechanical robustness of the 3D-nanostructured BDD microelectrodes after repetitive standard cleaning (see methods) and found no noticeable change in the noise level of the MEA (Fig. S3).

### 3.3. Neural recording and microstimulation

Both conventional and 3D-3 BDD microelectrodes were used for recording rhythmic activity from the whole embryonic hindbrain-spinal cord. Consistently with their high intrinsic noise (Fig. 3F), conventional BDD microelectrodes did not allow reliable recordings of the low-amplitude activity displayed by this preparation. By contrast, 3D-nanostructured BDD allowed the detection of episodes of activity propagating as waves from the hindbrain down the spinal cord (Fig. 4). These episodes could be recorded as LFPs on the 3D-nanostructured BDD microelectrodes covering the hindbrain (Fig. 4C and D). Bursts of spikes could be detected on 3D-nanostructured BDD microelectrodes along all the preparation, as shown in Fig. 4E. Noticeably, even small amplitude spiking signals (within the 10–20 μV range) could be clearly detected. Activity could also be triggered by applying a 1 ms biphasic (cathodic first) current of 10 μA through the 3D-nanostructured BDD microelectrodes located under the hindbrain. Fig. 4F shows the recording of a typical burst of spikes elicited by an electrical stimulation delivered by a BDD microelectrode and lasting about three hundreds milliseconds.

We also recorded spiking activity from a 14 DIV hippocampal cell culture on a few 20-μm-diameter 3D-nanostructured BDD microelectrodes of a 1 × 60 linear array with a 100-μm inter-electrode spacing (Fig. 5). Microelectrodes that recorded signals were generally the ones covered by a dense layer of cells (Fig. 5A). As shown in Fig. 5B, the activity recorded in these cultures mainly consists of bursts of spikes, including some with an amplitude

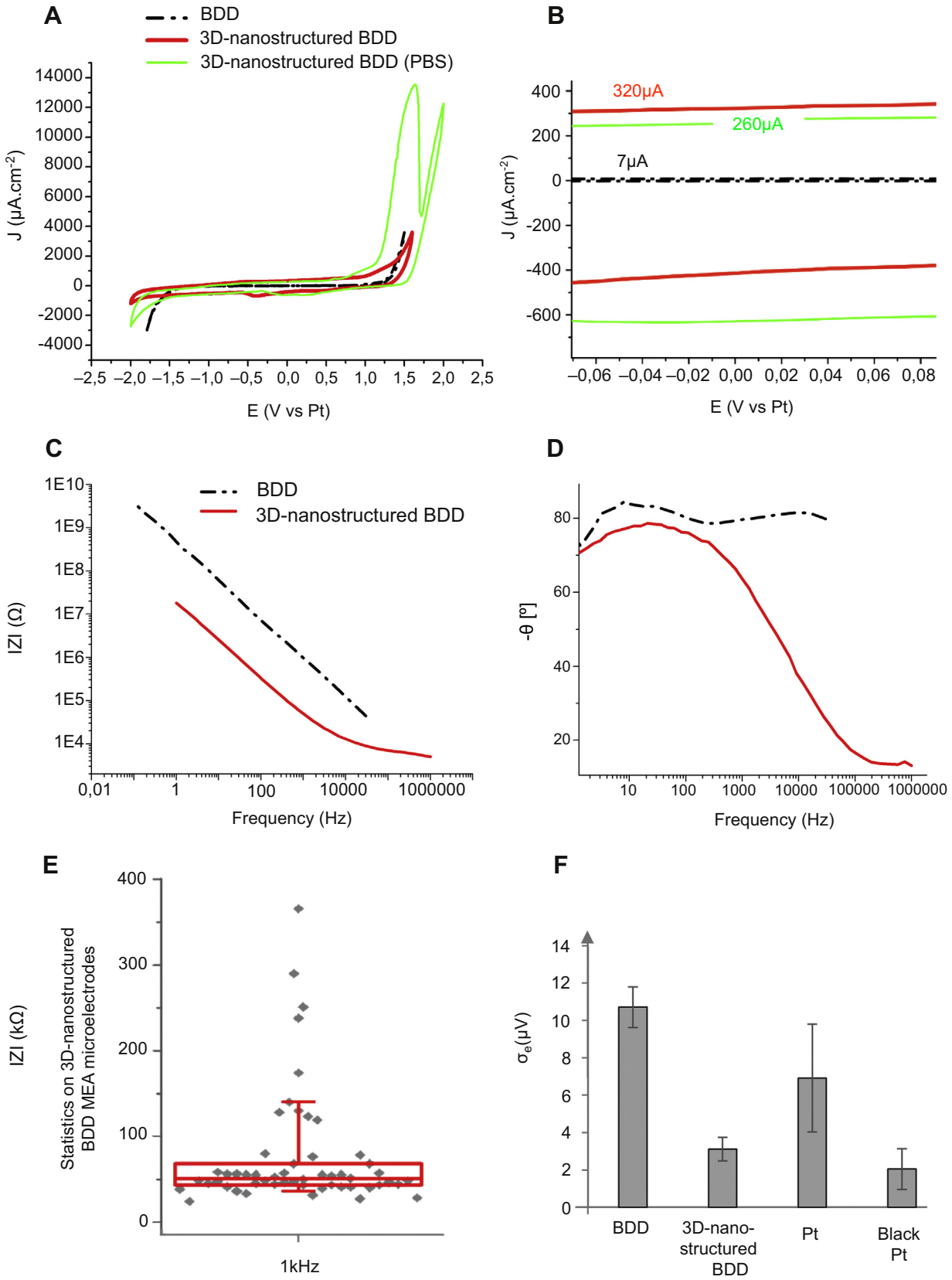


**Fig. 3.** Characterization of 20-µm-diameter BDD microelectrodes. A) Cyclic voltammetry at 100 mV $s^{-1}$ for BDD diamond (black dotted) in $LiClO_4$ and for 3D-nanostructured BDD diamond in $LiClO_4$ (red) and in PBS (green). B) A focus on the − 0.06 to +0.08 window for cyclic voltammetry at 100 mV $s^{-1}$ for BDD diamond (black dotted) in $LiClO_4$ and for 3D-nanostructured BDD diamond in $LiClO_4$ (red) and in PBS (green). C-D) Bode representation for one BDD microelectrode (black dotted) and one 3D-nanostructured BDD microelectrode (red) in $LiClO_4$ of C) the typical impedance spectra and of D) the typical phase spectra. E) Impedances of 3D-nanostructured BDD diamond microelectrodes in $LiClO_4$ at 1 KHz. F) Median ± standard deviation of the noise level recorded in aCSF for 60 microelectrodes with a 20-µm-diameter and made of conventional BDD, 3D-nanostructured BDD, platine (Pt), or black Pt. (For interpretation of the references to color in this figure legend, the reader is referred to the web version of this article.)

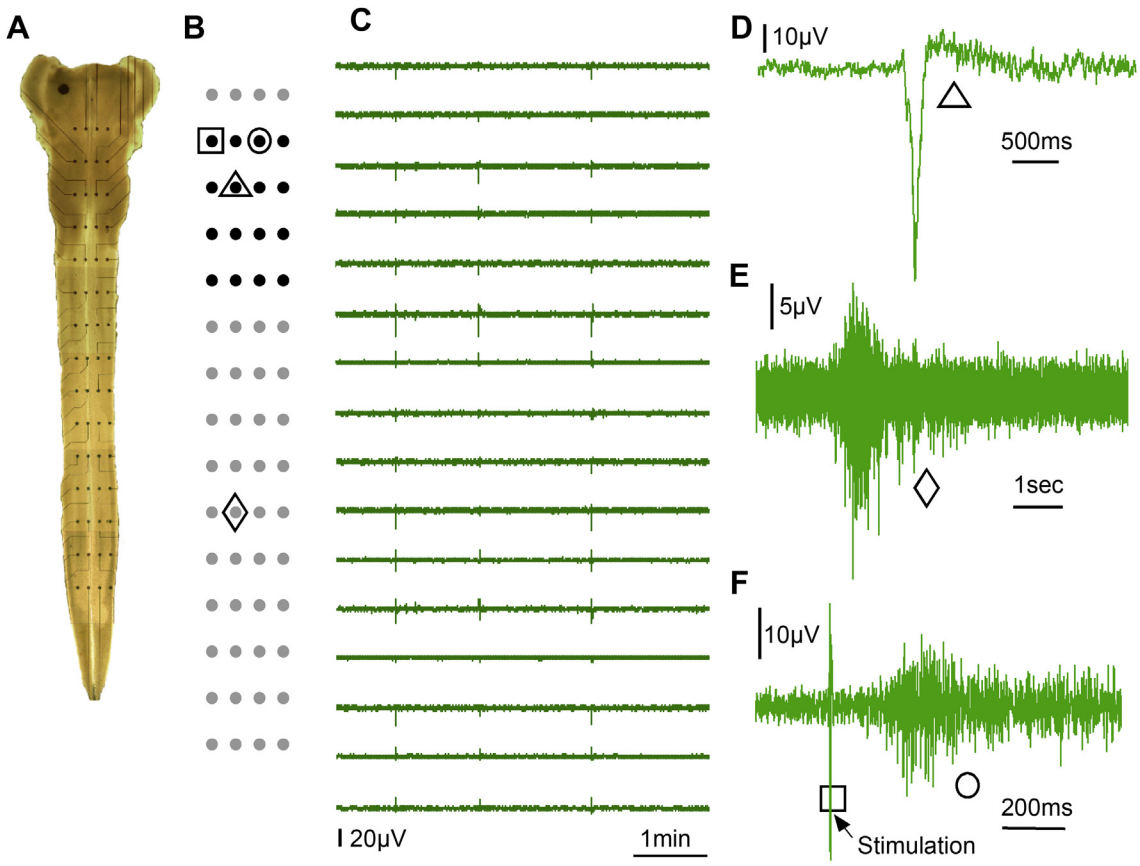


**Fig. 4.** A) Picture of the whole embryonic mouse hindbrain-spinal cord preparation opened on a 4 × 15 3D-nanostructured BDD MEA. B) Layout of the 4 × 15 3D-nanostructured BDD MEA. C) Five minutes recording showing three episodes of the rhythmic activity detected in the rostral region of the preparation by 16 3D-nanostructured BDD microelectrodes colored in black in B layout. D) A focus on an LFP recorded at the electrode marked with a triangle in B layout. E) Detail of a burst of spikes detected on the marked with a diamond in B layout for the third episode shown in C. F) Bursts of spikes recorded on electrode marked with a circle in B layout and triggered when applying a 1-ms biphasic (cathodic first) current of 10 μA on one microelectrode located in the upper medulla (electrode marked with a square in B layout).

below 10 μV. These are similar to those observed by Gavello et al. in their hippocampal cultures [74]. Also, the application of a 1-ms biphasic current of 10 μA typically triggered a multiunit response characterized by a burst of spikes (Fig. 5C).

## 4. Discussion

To date, although BDD displays excellent biocompatibility [30–32,35,37], chemical inertness [40], and structural stability [41,42] properties, it has been poorly considered for neural application and there is no report for low-noise neural recording and stimulation with BDD microelectrode arrays [66–68,75]. Indeed, the intrinsic impedance and capacitance of conventional BDD do not match those of its competitor materials. Here however, we fabricated MEAs with 3D-nanostructured BDD microelectrodes (20-μm-diameter) and found that this material provides good performance for neural recording and stimulation.

We found interface impedance of 3D-nanostructured BDD microelectrodes 40 times lower than that of conventional BDD microelectrodes, a result consistent with observations previously reported on larger macroelectrodes [49]. This improvement can be explained by the increased surface area available on the microelectrode due to its nanostructuration [52,76]. Moreover, the microelectrode surfaces consist of a BDD layer deposited on a template of vertically aligned carbon nanotube (VACNT). The vertical CNT inter-layer has the advantage to be highly conductive, thus acting as an efficient current collector and ensuring a high conductivity through the thickness of the electrode [77]. Altogether, the porosity and resulting enhanced conductivity of 3D-nanostructured BDD microelectrodes explain their much lower impedances compared to microelectrodes made of conventional BDD. The median impedance at 1 kHz, the current standard frequency to evaluate the electrode performance corresponding to the main spike event frequency, was found to be of 50 kΩ for 20-μm-diameter microelectrodes. This value remains comparable to values obtained for current state of the art neural electrode materials such as titanium nitride (TiN) [50 kΩ for 30-μm-diameter electrodes, [78]], poly(3,4-éthylènedioxythiophène) (PEDOT) and PEDOT-CNT [20 kΩ for 30-μm-diameter electrodes, [79]], iridium oxide (IrOx) [14 kΩ for 100-μm-diameter electrodes,[80]], and black Pt [80 kΩ for 12-μm-diameter electrodes, [28]].

As a consequence of the low impedance level of these 3D-nanostructured BDD microelectrodes, we found that their noise level was notably reduced in comparison to conventional BDD MEAs. This low intrinsic noise level allows the detection of small amplitude signals in the range of 10–20 μV in both types of neural preparations tested in the study. In the hippocampal cell culture recording, microelectrodes recording signals were generally the ones covered by a dense layer of cells. This is in line with previous studies characterizing MEA recording of dissociated cell cultures [81]. Our results show that when compared with black platinum electrodes with identical diameter, 3D-nanostructured BDD exhibits higher intrinsic noise. However, black platinum microelectrodes are highly friable [28], while the 3D-nanostructured BDD MEA were very robust and reusable several times.

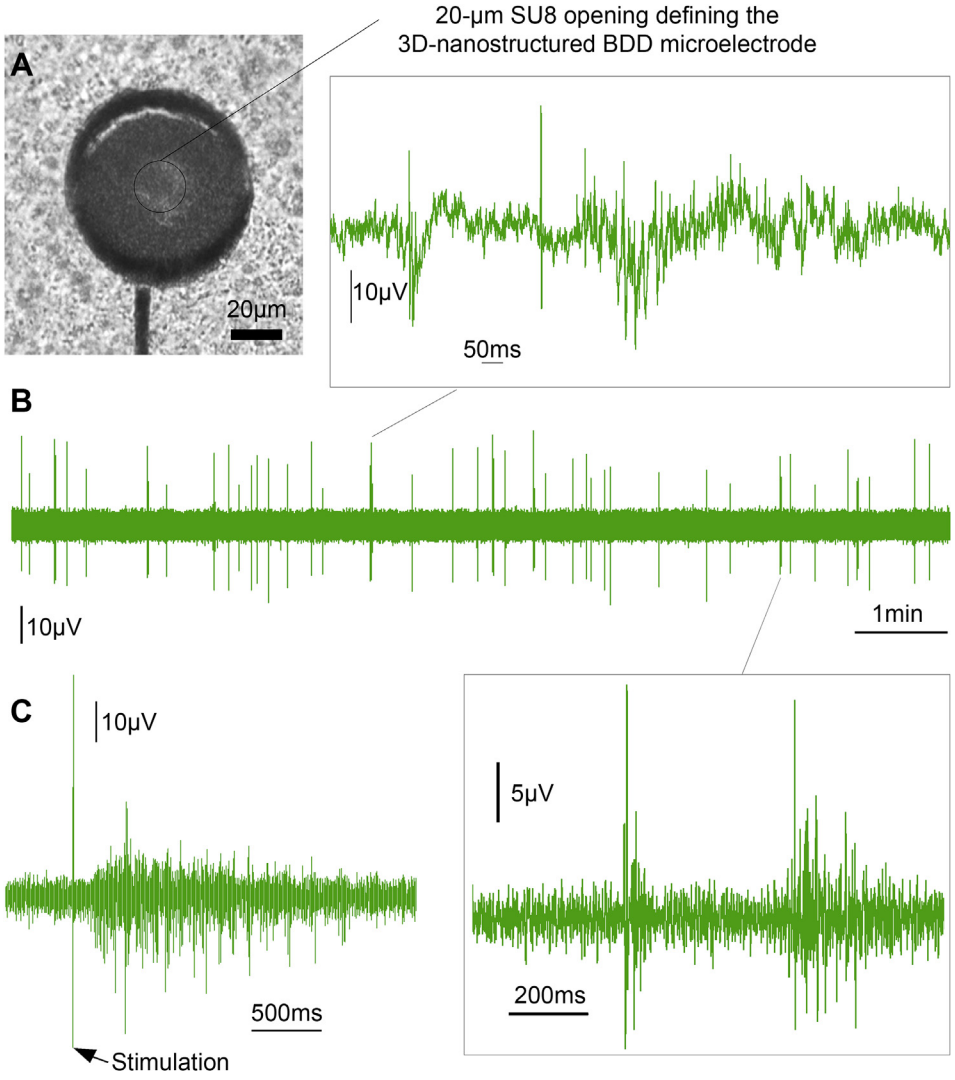


**Fig. 5.** A) Picture of a 3D-nanostructured BDD microelectrode covered with 14 DIV hippocampal cells. B) 10 min recording (middle) showing the 14 DIV hippocampal cell activity detected by one BDD microelectrode with two close-up views on bursts of spikes. C) Bursts of spikes (bottom right) triggered when applying a 1 ms biphasic current of 10 µA to a 3D-nanostructured BDD microelectrode.

Further electrochemical performances of the electrodes were characterized by cyclic voltammetry both in $LiClO_4$ and in PBS. The composition of the first electrolyte is typical for characterizing the potential window of an electrode, while the second is a physiological medium. The potential window of the diamond, typically of 3 V, was not altered during the MEA micro-fabrication steps, in the case of neither conventional nor 3D-nanostructured BDD. This large potential window is a strong asset to limit electrochemical reaction of water hydrolysis when the microelectrode is driven to high potential values. This is important to ensure safe charge injection avoiding harmful reactions during electrical neural stimulation, and particularly with microelectrodes of small sizes and thus subject to higher charge density thresholds [29].

The CV measurements allowed to estimate the gain in developed surface via the ratio of the capacitive currents measured on the 3D-nanostructured versus conventional BDD microelectrodes. An increase factor of 43 was found (3 mF $cm^{-2}$ versus 70 µF $cm^{-2}$) in coherence with the factor of 40 previously reported for large surface electrode [49]. The theoretical charge storage capacity (CSC) of 3D-nanostructured BDD was deduced to be of about 10 mC $cm^{-2}$, a value higher than values reported for TiN [0.9 mC $cm^{-2}$, for 70-µm-diameter electrodes, [82]], and below than values reported for IrOx [28 mC $cm^{-2}$, for ~20-µm-diameter electrodes, [83]] or PEDOT [75 mC $cm^{-2}$ for ~20-µm-diameter electrodes, [83]].

Most employed charge-injection electrodes present three main types of charge-injection mechanisms [29]. Among the modelled materials, titanium nitride is a chemically stable metallic conductor that presents a wide potential window −0.9 to 0.9 V with no irreversible reactions and thus uses a capacitive mechanism. Iridium oxide instead goes through a faradaic mechanism exploiting the hydrated oxide film created via the reversible reaction of iridium oxidation and reduction. Platinum displays a pseudo-capacitive mechanism where faradaic surface reactions of oxide formation and hydrogen atom plating as well as double layer charging play a role in most neural stimulation conditions. CV measurement in PBS evidenced a large peak beyond a potential of +1.3 V suggesting that the 3D-nanostructured BDD microelectrode undergoes an electrochemical reaction at high positive potentials. This phenomenon has been observed previously for conventional BDD in $NaClO_4$ [41] and for platinum in PBS [84] that was respectively attributed to an oxidation of the BDD and to the presence of the chloride ion $Cl^-$. In our case, this peak can mostly be associated to the chloride ion

present in PBS and aCSF since the peak is not visible when CV measurements are performed in a phosphate buffer free of NaCl. Though, the charge injection mechanism for 3D-nanostructured BDD may remain capacitive within a very wide window −1.5 to +1.1 V where no reactions took place. This is a much larger window and a much greater CSC of 6.8 mC $cm^{-2}$ than that of TiN.

A critical aspect for an electrode material is to avoid, at the electrode-tissue interface, not only the electrochemical reactions during charge injection [29], but also other chemical reactions occurring during passive use of the electrode and leading to long-term material degradation, a further concern for long-term recordings [6]. In comparison to conducting polymers [51,85] and most metals [86–88], diamond and CNT display far better chemical stability. Diamond erosion only takes place in severe conditions that include very high temperatures, much above 37 °C, or when submitted to high current densities [41]. Also, although CNT is a chemically robust nanomaterial, the potential release of single CNTs or CNT bundles from the electrode in the tissue and their toxicity is not well known and can be a concern for clinical applications [89]. In such case, it should be noted that other strategies for BDD nanostructuration could further be envisioned. Yet, in our 3D-nanostructured BDD electrode approach, CNTs were firmly encapsulated between two BDD layers. The embryonic neural cell culture indicated that neurons could attach, survive, and grow neurites on 3D-nanostructured BDD surfaces, with no visible difference in neurite extension. The biocompatibility of BDD surfaces was already assessed with different cell types, among which neural cells [31–36,38]. Our results thus confirm the suitability of BDD for neural cell cultures. It could have been expected however that the 3D-nanostructured BDD surfaces would lead to a greater neurite extension compared to the conventional BDD surface. Indeed, CNT have been shown to promote the neurite extension [57,90,91]. Also, the role of the geometry of nanostructures in neurite outgrowth was evidenced in numerous studies [56,92–94]. Since BDD surfaces are actually not smooth surfaces (see Fig. 2A), it is possible that their morphology already favors the neurite outgrowth [36,38]. 3D-nanostructured BDD thus appears as a reliable and powerful material for neural interfaces, which should be investigated and characterized further with in vivo studies.

## 5. Conclusion

In conclusion, our results demonstrate that 3D-nanostructured BDD offers good performances for neural recording and stimulation. The impedance of 20-μm-diameter microelectrodes were found to be 50 kΩ at 1 KHz, which is comparable to values obtained for current state-of-the-art neural microelectrode materials. These new MEAs also display a high safe charge injection capacity as they combine advantages of the large electrochemical potential window of diamond with the large surface area provided by nanostructuration. The MEA ability in stimulating and recording low amplitude neural signals, together with the established diamond biostability and biocompatibility, should significantly benefit to the future development of new types of MEA-based neural prostheses and implants for the exploration and rehabilitation of the nervous system.

## Acknowledgments

We would like to emphasize and acknowledge the strong initial contribution to this work of Mathias Bonnauron, who deceased on February 5th, 2008 in a ski accident. We would like to thank Lauriane Hamard for her help in dissecting embryonic hippocampi. We gratefully acknowledge the financial support of this study by the French Agence Nationale de la Recherche (ANR) through the project MEDINAS (ANR07TECSAN014), INSERM, UPMC (Paris VI), the Fondation Ophtalmologique A. de Rothschild (Paris), the Fédération des Aveugles de France, IRRP, the city of Paris, the Regional Council of Ile-de-France. We also gratefully acknowledge the NEUROCARE project from the European Community's Seventh Framework Programme (FP7/2007-2013) under grant agreement n° 280433.

## Appendix A. Supplementary data

Supplementary data related to this article can be found at http://dx.doi.org/10.1016/j.biomaterials.2015.02.021.

## References

[1] Kennedy PR. The cone electrode: a long-term electrode that records from neurites grown onto its recording surface. J Neurosci Methods 1989;29:181–93.
[2] Kennedy PR. Restoration of neural output from a paralyzed patient by a direct brain connection. Neuroreport 1998:9.
[3] Rothschild RM. Neuroengineering tools/applications for bidirectional interfaces, brain computer interfaces, and neuroprosthetic implants – a review of recent progress. Front Neuroeng 2010;3.
[4] Borton DA, Yin M, Aceros J, Nurmikko A. An implantable wireless neural interface for recording cortical circuit dynamics in moving primates. J Neural Eng 2013;10. 026010.
[5] Fattahi P, Yang G, Kim G, Abidian MR. A review of organic and inorganic biomaterials for neural interfaces. Adv Mater 2014;26:1846–85.
[6] Barrese JC, Rao N, Paroo K, Triebwasser C, Vargas-Irwin C, Franquemont L, et al. Failure mode analysis of silicon-based intracortical microelectrode arrays in non-human primates. J Neural Eng 2013;10. 066014.
[7] Clark GM, Tong YC, Black R, Forster IC, Patrick JF, Dewhurst DJ. A multiple electrode cochlear implant. J Laryngol Otol 1977;91:935–45.
[8] Benabid AL, Pollak P, Gervason C, Hoffmann D, Gao DM, Hommel M, et al. Long-term suppression of tremor by chronic stimulation of the ventral intermediate thalamic nucleus. Lancet 1991;337:403–6.
[9] Weiland JD, Liu W, Humayun MS. Retinal prosthesis. Annu Rev Biomed Eng 2005;7:361–401.
[10] Lorach H, Marre O, Sahel J-A, Benosman R, Picaud S. Neural stimulation for visual rehabilitation: advances and challenges. J Physiol Paris 2013 Nov;107(5):421–31.
[11] Hochberg LR, Bacher D, Jarosiewicz B, Masse NY, Simeral JD, Vogel J, et al. Reach and grasp by people with tetraplegia using a neurally controlled robotic arm. Nature 2012;485.
[12] Hochberg LR, Serruya MD, Friehs GM, Mukand JA, Saleh M, Caplan AH, et al. Neuronal ensemble control of prosthetic devices by a human with tetraplegia. Nature 2006;442:164–71.
[13] Moritz CT, Perlmutter SI, Fetz EE. Direct control of paralysed muscles by cortical neurons. Nature 2008;456:639–42.
[14] Wessberg J, Stambaugh CR, Kralik JD, Beck PD, Laubach M, Chapin JK, et al. Real-time prediction of hand trajectory by ensembles of cortical neurons in primates. Nature 2000;408:361–5.
[15] Collinger JL, Wodlinger B, Downey JE, Wang W, Tyler-Kabara EC, Weber DJ, et al. High-performance neuroprosthetic control by an individual with tetraplegia. Lancet 2013;381:557–64.
[16] Csicsvari J, Henze DA, Jamieson B, Harris KD, Sirota A, Bartho P, et al. Massively parallel recording of unit and local field potentials with silicon-based electrodes. J Neurophysiol 2003;90:1314–23.
[17] Maynard EM, Nordhausen CT, Normann RA. The Utah intracortical electrode array: a recording structure for potential brain-computer interfaces. Electroencephalogr Clin Neurophysiol 1997;102:228–39.
[18] Nicolelis MA, Dimitrov D, Carmena JM, Crist R, Lehew G, Kralik JD, et al. Chronic, multisite, multielectrode recordings in macaque monkeys. Proc Natl Acad Sci U. S. A 2003;100:11041–6.
[19] Wise KD, Anderson DJ, Hetke JF, Kipke DR, Najafi K. Wireless implantable microsystems: high-density electronic interfaces to the nervous system. Proc IEEE 2004;92:76–97.
[20] Mathieson K, Loudin J, Goetz G, Huie P, Wang L, Kamins TI, et al. Photovoltaic retinal prosthesis with high pixel density. Nat Photonics 2012;6:391–7.
[21] Nirenberg S, Pandarinath C. Retinal prosthetic strategy with the capacity to restore normal vision. Proc Natl Acad Sci 2012;109:15012–7.
[22] Charvet G, Rousseau L, Billoint O, Gharbi S, Rostaing J-P, Joucla S, et al. BioMEATM: a versatile high-density 3D microelectrode array system using integrated electronics. Biosens Bioelectron 2010;25:1889–96.
[23] Béduer A, Joris P, Mosser S, Delattre V, Fraering PC, Renaud P. Accurate resistivity mouse brain mapping using microelectrode arrays. Biosens Bioelectron 2014;60:143–53.
[24] Berdondini L, Imfeld K, Maccione A, Tedesco M, Neukom S, Koudelka-Hep M, et al. Active pixel sensor array for high spatio-temporal resolution

electrophysiological recordings from single cell to large scale neuronal networks. Lab Chip 2009;9:2644–51.
[25] Berdondini L, van der Wal PD, Guenat O, de Rooij NF, Koudelka-Hep M, Seitz P, et al. High-density electrode array for imaging in vitro electrophysiological activity. Biosens Bioelectron 2005;21:167–74.
[26] Frey U, Egert U, Heer F, Hafizovic S, Hierlemann A. Microelectronic system for high-resolution mapping of extracellular electric fields applied to brain slices. Biosens Bioelectron 2009;24:2191–8.
[27] Hutzler M, Lambacher A, Eversmann B, Jenkner M, Thewes R, Fromherz P. High-resolution multitransistor array recording of electrical field potentials in cultured brain slices. J Neurophysiol 2006;96:1638–45.
[28] Heim M, Rousseau L, Reculusa S, Urbanova V, Mazzocco C, Joucla S, et al. Combined macro-/mesoporous microelectrode arrays for low-noise extracellular recording of neural networks. J Neurophysiol 2012;108:1793–803.
[29] Cogan SF. Neural stimulation and recording electrodes. Annu Rev Biomed Eng 2008;10:275–309.
[30] Grill A. Diamond-like carbon coatings as biocompatible materials—an overview. Diam Relat Mater 2003;12:166–70.
[31] Tang L, Tsai C, Gerberich WW, Kruckeberg L, Kania DR. Biocompatibility of chemical-vapour-deposited diamond. Biomaterials 1995;16:483–8.
[32] Specht CG, Williams OA, Jackman RB, Schoepfer R. Ordered growth of neurons on diamond. Biomaterials 2004;25:4073–8.
[33] Lechleitner T, Klauser F, Seppi T, Lechner J, Jennings P, Perco P, et al. The surface properties of nanocrystalline diamond and nanoparticulate diamond powder and their suitability as cell growth support surfaces. Biomaterials 2008;29:4275–84.
[34] Kelly S, Regan EM, Uney JB, Dick AD, McGeehan JP, Mayer EJ, et al. Patterned growth of neuronal cells on modified diamond-like carbon substrates. Biomaterials 2008;29:2573–80.
[35] Chen YC, Lee DC, Hsiao CY, Chung YF, Chen HC, Thomas JP, et al. The effect of ultra-nanocrystalline diamond films on the proliferation and differentiation of neural stem cells. Biomaterials 2009;30:3428–35.
[36] Edgington RJ, Thalhammer A, Welch JO, Bongrain A, Bergonzo P, Scorsone E, et al. Patterned neuronal networks using nanodiamonds and the effect of varying nanodiamond properties on neuronal adhesion and outgrowth. J Neural Eng 2013;10. 056022.
[37] May PW, Regan EM, Taylor A, Uney J, Dick AD, McGeehan J. Spatially controlling neuronal adhesion on CVD diamond. Diam Relat Mater 2012;23:100–4.
[38] Babchenko O, Romanyuk N, Jendelova P, Kromka A. Tailoring morphologies of diamond thin films for neural stem cells culturing. Phys Status Solidi 2013;250:2717–22.
[39] Bendali A, Agnès C, Meffert S, Forster V, Bongrain A, Arnault J-C, et al. Distinctive glial and neuronal interfacing on nanocrystalline diamond. PLoS One 2014;9. e92562.
[40] Hupert M, Muck A, Wang J, Stotter J, Cvackova Z, Haymond S, et al. Conductive diamond thin-films in electrochemistry. Diam Relat Mater 2003;12:1940–9.
[41] Chaplin BP, Hubler DK, Farrell J. Understanding anodic wear at boron doped diamond film electrodes. Electrochim Acta 2013;89:122–31.
[42] Chen Q, Granger MC, Lister TE, Swain GM. Morphological and microstructural stability of boron-doped diamond thin film electrodes in an acidic chloride medium at high anodic current densities. J Electrochem Soc 1997;144:3806–12.
[43] Carabelli V, Gosso S, Marcantoni A, Xu Y, Colombo E, Gao Z, et al. Nanocrystalline diamond microelectrode arrays fabricated on sapphire technology for high-time resolution of quantal catecholamine secretion from chromaffin cells. Biosens Bioelectron 2010;26:92–8.
[44] Gosso S, Turturici M, Franchino C, Colombo E, Pasquarelli A, Carbone E, et al. Heterogeneous distribution of exocytotic microdomains in adrenal chromaffin cells resolved by high-density diamond ultra-microelectrode arrays. J Physiol 2014;592:3215–30.
[45] Panizza M, Michaud PA, Cerisola G, Comninellis C. Anodic oxidation of 2-naphthol at boron-doped diamond electrodes. J Electroanal Chem 2001;507:206–14.
[46] Halpern JM, Xie S, Sutton GP, Higashikubo BT, Chestek CA, Lu H, et al. Diamond electrodes for neurodynamic studies in Aplysia californica. Diam Relat Mater 2006;15:183–7.
[47] Park J, Quaiserová-Mocko V, Pecková K, Galligan JJ, Fink GD, Swain GM. Fabrication, characterization, and application of a diamond microelectrode for electrochemical measurement of norepinephrine release from the sympathetic nervous system. Diam Relat Mater 2006;15:761–72.
[48] Garrett DJ, Ganesan K, Stacey A, Fox K, Meffin H, Prawer S. Ultra-nanocrystalline diamond electrodes: optimization towards neural stimulation applications. J Neural Eng 2012;9. 1741–2560.
[49] Hébert C, Mazellier JP, Scorsone E, Mermoux M, Bergonzo P. Boosting the electrochemical properties of diamond electrodes using carbon nanotube scaffolds. Carbon 2014;71:27–33.
[50] Wang K, Fishman HA, Dai H, Harris JS. Neural stimulation with a carbon nanotube microelectrode array. Nano Lett 2006;6:2043–8.
[51] Bareket-Keren L, Hanein Y. Carbon nanotube-based multi electrode arrays for neuronal interfacing: progress and prospects. Front Neural Circuits 2012;6:122.
[52] Heim M, Yvert B, Kuhn A. Nanostructuration strategies to enhance microelectrode array (MEA) performance for neuronal recording and stimulation. J Physiol 2012;106:137–45.
[53] Abidian MR, Martin DC. Experimental and theoretical characterization of implantable neural microelectrodes modified with conducting polymer nanotubes. Biomaterials 2008;29:1273–83.
[54] Abidian MR, Corey JM, Kipke DR, Martin DC. Conducting-polymer nanotubes improve electrical properties, mechanical adhesion, neural attachment, and neurite outgrowth of neural electrodes. Small 2010;6:421–9.
[55] Shoval A, Adams C, David-Pur M, Shein M, Hanein Y, Sernagor E. Carbon nanotube electrodes for effective interfacing with retinal tissue. Front Neuroeng 2009;2:4.
[56] Piret G, Perez MT, Prinz CN. Neurite outgrowth and synaptophysin expression of postnatal CNS neurons on GaP nanowire arrays in long-term retinal cell culture. Biomaterials 2013;34:875–87.
[57] Gottipati MK, Kalinina I, Bekyarova E, Haddon RC, Parpura V. Chemically functionalized water-soluble single-walled carbon nanotubes modulate morpho-functional characteristics of astrocytes. Nano Lett 2012;12:4742–7.
[58] McKenzie JL, Waid MC, Shi R, Webster TJ. Decreased functions of astrocytes on carbon nanofiber materials. Biomaterials 2004;25:1309–17.
[59] Ereifej ES, Cheng MM-C, Mao G, VandeVord PJ. Examining the inflammatory response to nanopatterned polydimethylsiloxane using organotypic brain slice methods. J Neurosci Methods 2013;217:17–25.
[60] Ereifej ES, Matthew HW, Newaz G, Mukhopadhyay A, Auner G, Salakhutdinov I, et al. Nanopatterning effects on astrocyte reactivity. J Biomed Mater Res A 2013;101:1743–57.
[61] Tysseling-Mattiace VM, Sahni V, Niece KL, Birch D, Czeisler C, Fehlings MG, et al. Self-assembling nanofibers inhibit glial scar formation and promote axon elongation after spinal cord injury. J Neurosci 2008;28:3814–23.
[62] Zarbin MA, Montemagno C, Leary JF, Ritch R. Nanotechnology in ophthalmology. Can J Ophthalmol/J Can d'Ophtalmologie 2010;45:457–76.
[63] Redenti S, Tao S, Yang J, Gu P, Klassen H, Saigal S, et al. Retinal tissue engineering using mouse retinal progenitor cells and a novel biodegradable, thin-film poly(e-caprolactone) nanowire scaffold. J Ocul Biol Dis Infor 2008;1:19–29.
[64] Gelain F, Panseri S, Antonini S, Cunha C, Donega M, Lowery J, et al. Transplantation of nanostructured composite scaffolds results in the spinal cords 2011;5:227–36.
[65] Pal A, Singh A, Nag TC, Chattopadhyay P, Mathur R, Jain S. Iron oxide nanoparticles and magnetic field exposure promote functional recovery by attenuating free radical-induced damage in rats with spinal cord transection. Int J Nanomedicine 2013;8:2259–72.
[66] Ariano P, Lo Giudice A, Marcantoni A, Vittone E, Carbone E, Lovisolo D. A diamond-based biosensor for the recording of neuronal activity. Biosens Bioelectron 2009;24:2046–50.
[67] Chan HY, Aslam DM, Wiler JA, BC. A novel diamond microprobe for neurochemical and -electrical recording in neural prosthesis. JMEMS 2009;18:511–21.
[68] Gosso S, Marcantoni A, Turturici M, Pasquarelli A, Carbone E, VC. Multi-purpose nanocrystalline boron-doped diamond MEAs for amperometric, potentiometric and pH recordings from excitable cells. MEA Meet Proc 2012:323–4.
[69] Vanhove E, de Sanoit J, Mailley P, Pinault M-A, Jomard F, Bergonzo P. High reactivity and stability of diamond electrodes: the influence of the B-doping concentration. Phys Status Solidi 2009;206:2063–9.
[70] Girard HA, Perruchas S, Gesset C, Chaigneau M, Vieille L, Arnault J-C, et al. Electrostatic grafting of diamond nanoparticles: a versatile route to nanocrystalline diamond thin films. ACS Appl Mater Interfaces 2009;1:2738–46.
[71] Scorsone E, Saada S, Arnault JC, Bergonzo P. Enhanced control of diamond nanoparticle seeding using a polymer matrix. J Appl Phys 2009;106:14906–8.
[72] Yvert B, Mazzocco C, Joucla S, Langla A, Meyrand P. Artificial CSF motion ensures rhythmic activity in the developing CNS ex vivo: a mechanical source of rhythmogenesis? J Neurosci 2011;31:8832–40.
[73] Hébert C, Warnking J, Depaulis A, Garçon LA, Mermoux M, Eon D, et al. Microfabrication, characterization and in vivo MRI compatibility of diamond microelectrodes array for neural interfacing. Mater Sci Eng C 2015;46:25–31.
[74] Gavello D, Rojo-Ruiz J, Marcantoni A, Franchino C, Carbone E, Carabelli V. Leptin counteracts the hypoxia-induced inhibition of spontaneously firing hippocampal neurons: a microelectrode array study. PLoS One 2012;7. e41530.
[75] Keefer EW, Botterman BR, Romero MI, Rossi AF, Gross GW. Carbon nanotube coating improves neuronal recordings. Nat Nano 2008;3:434–9.
[76] Delpy A, Allain A-E, Meyrand P, Branchereau P. NKCC1 cotransporter inactivation underlies embryonic development of chloride-mediated inhibition in mouse spinal motoneuron. J Physiol 2008;586:1059–75.
[77] Nguyen-Vu TDB, Chen H, Cassell AM, Andrews R, Meyyappan M, Li J. Vertically aligned carbon nanofiber arrays: an advance toward electrical-neural interfaces. Small 2006;2:89–94.
[78] Egert U, Schlosshauer B, Fennrich S, Nisch W, Fejtl M, Knott T, et al. A novel organotypic long-term culture of the rat hippocampus on substrate-integrated multielectrode arrays. Brain Res Brain Res Protoc 1998;2:229–42.
[79] Gerwig R, Fuchsberger K, Schroeppel B, Link GS, Heusel G, Kraushaar U, et al. PEDOT-cnt composite microelectrodes for recording and electrostimulation applications: fabrication, morphology, and electrical properties. Front Neuroeng 2012;5:8.
[80] Eick S, Wallys J, Hofmann B, van Ooyen A, Schnakenberg U, Ingebrandt S, et al. Iridium oxide microelectrode arrays for in vitro stimulation of individual rat neurons from dissociated cultures. Front Neuroeng 2009;2:16.
[81] Wagenaar DA, Pine J, Potter SM. An extremely rich repertoire of bursting patterns during the development of cortical cultures. BMC Neurosci 2006;7:11.

[82] Weiland JD, Anderson DJ, Humayun MS. In vitro electrical properties for iridium oxide versus titanium nitride stimulating electrodes. IEEE Trans Biomed Eng 2002;49:1574–9.
[83] Wilks SJ, Richardson-burns SM, Hendricks JL, Martin DC, Otto KJ. Poly ( 3, 4-ethylenedioxythiophene ) as a micro-neural interface material for electrostimulation 2009;2:1–8.
[84] Hudak EM, Mortimer JT, Martin HB. Platinum for neural stimulation: voltammetry considerations. J Neural Eng 2010;7:26005.
[85] Yamato H, Ohwa M, Wernet W. Stability of polypyrrole and poly(3,4-ethylenedioxythiophene) for biosensor application. J Electroanal Chem 1995;397:163–70.
[86] McHardy J, Robblee LS, Marston JM, Brummer SB. Electrical stimulation with pt electrodes. IV. Factors influencing Pt dissolution in inorganic saline. Biomaterials 1980;1:129–34.
[87] Robblee LS, McHardy J, Marston JM, Brummer SB. Electrical stimulation with Pt electrodes. V. The effect of protein on Pt dissolution. Biomaterials 1980;1:135–9.
[88] Black RC, Hannaker P. Dissolution of smooth platinum electrodes in biological fluids. Appl Neurophysiol 1980;42:366–74.
[89] Kaiser J-P, Roesslein M, Buerki-Thurnherr T, Wick P. Carbon nanotubes – curse or blessing. Curr Med Chem 2011;18:2115–28.
[90] Matsumoto K, Sato C, Naka Y, Whitby R, Shimizu N. Stimulation of neuronal neurite outgrowth using functionalized carbon nanotubes. Nanotechnology 2010;21. 115101.
[91] Fabbro A, Villari A, Laishram J, Scaini D, Toma FM, Turco A, et al. Spinal cord explants use carbon nanotube interfaces to enhance neurite outgrowth and to fortify synaptic inputs. ACS Nano 2012;6:2041–55.
[92] Hallstrom W, Martensson T, Prinz C, Gustavsson P, Montelius L, Samuelson L, et al. Gallium phosphide nanowires as a substrate for cultured neurons. Nano Lett 2007;7:2960–5.
[93] Hallstrom W, Prinz CN, Suyatin D, Samuelson L, Montelius L, Kanje M. Rectifying and sorting of regenerating axons by free-standing nanowire patterns: a highway for nerve fibers. Langmuir 2009;25:4343–6.
[94] Piret G, Perez M-T, Prinz CN. Substrate porosity induces phenotypic alterations in retinal cells cultured on silicon nanowires. RSC Adv 2014;4:27888–97.